Spin-orbit torque modulated by interface chemistry in topological BiSb/NiFe bilayers with titanium insertion

Talluri Manoj,[1,2] Zhenchao Wen,[1] Jun Uzuhashi,[1] Tadakatsu Ohkubo,[1] Hiroaki Sukegawa,[1] Chandrasekhar Murapaka,[2] Brian York,[3] Xiaoyong Liu,[3] Quang Le,[3] and Seiji Mitani[1]*

[1]National Institute for Materials Science, Tsukuba 305-0047, Japan.

[2]Department of Materials Science and Metallurgical Engineering, Indian Institute of Technology-Hyderabad, 502284, Telangana, India

[3]Western Digital, San Jose, CA 95119, USA

*Wen.Zhenchao@nims.go.jp

KEYWORDS: topological insulator, BiSb, spin-orbit torque efficiency, Ti insertion, interface chemistry

ABSTRACT

Topological insulators are intriguing materials in the field of spintronics because they exhibit unique electronic properties that hold great promise for device applications. BiSb has attracted more research interest among topological materials due to its remarkably high spin-orbit torque (SOT) efficiency. However, due to the low melting point of the alloy, high diffusivities of Bi/Sb tend to degrade the SOT efficiency with temperature and aging. In this work, we utilize interfacial chemistry driven by a titanium (Ti) spacer between BiSb/NiFe bilayers to improve the SOT efficiency. We investigated the effect of the Ti insertion layer on the SOT efficiency in as-deposited, room-temperature aging, and annealing conditions. The SOT efficiency, estimated from the spin-torque ferromagnetic resonance response, revealed that the samples with the Ti layer had shown a multi-fold increase in the SOT efficiency compared to those without Ti insertion. Atomic resolution microstructural analyses provided a clear understanding of the interfacial chemistry where the Ti successfully hindered the interdiffusion of Ni and Sb. The interfacial chemistry in the vicinity of Ti contributed significantly to the improvement of the SOT efficiency. These results highlight the importance of the Ti insertion layer in the BiSb-based topological material/ferromagnet bilayer systems for SOT applications in spintronics.

INTRODUCTION

Topological insulators (TIs) are a compelling class of materials characterized by an insulating bulk bandgap and topologically protected gapless topological surface states (TSS).[1] The presence of Dirac points in their band structure endows TIs with exceptional surface conductivity,[2–4] making them versatile candidates for applications in various fields, including quantum computing, topological photonics, energy-efficient electronics, and more importantly in the field of spintronics.[5,6] The importance of TIs to spintronics lies in their properties to enable efficient spin transport, manipulation, and detection, which is fundamental to the development of advanced spin-based devices with notable energy efficiency, enhanced performance and functionality.[7] Within the realm of spintronics, the emergence of spin-orbit torque magnetic random access memories (SOT-MRAMs) and SOT readers beyond 4 Tb/in^2 magnetic recording technology has garnered extensive attention for the potential as an energy-efficient solution for neuromorphic computing and data storage.[8–11] In SOT-based devices, the most important layer is the spin Hall layer, which converts charge current to spin current through a phenomenon known as the spin Hall effect (SHE); and vice versa, i.e., spin flow is converted to charge current through the inverse spin Hall effect (ISHE).[9,12,13] Beyond conventional heavy metals,[14,15] some of the topological materials have been studied as spin - to-charge conversion systems in the SOT devices, such as BiSb,[16,17] Bi_2Se_3,[18–20] and Bi_2Te_3,[21] which exhibit high spin Hall angles (SHAs) or SOT efficiencies due to their strong spin-orbit coupling and topological electronic structures.

In the SOT technologies, however, the SOT efficiency and the conductivity of the spin Hall material play a major role in determining the device performance.[22–24] Despite the remarkable SHA values exhibited by TIs, their widespread utilization in spintronics is impeded by certain challenges. Notably, difficulties in deposition and low bulk conductivity have limited the applications of TIs, such as SOT-MRAMs, in thin film development using industrially employed sputtering deposition techniques on Si/SiO$_2$ substrates.[25] Previous reports indicate that the deposition of TIs is challenging due to their low melting point, leading to high deposition rates and the formation of non-uniform films with elevated roughness.[5,26–28] Among the various TIs, BiSb has gained much attention due to its large efficiency of spin-charge conversion and relatively high conductivity due to its particular TSS.[17] BiSb typically crystallizes in a rhombohedral A7 crystal structure with a specific ordered arrangement of Bi and Sb atoms, as shown in Figure 1(a). However, the low melting point of the BiSb alloy[29] raises concerns about Bi/Sb diffusion and phase separation, which could compromise SOT efficiency during annealing and even room temperature (RT) aging.[30,31] Also, the TSS of BiSb thin films was reported to be significantly affected by the selection of adjacent layers.[27,32–34] To date, it still remains a critical aspect requiring further investigation of the phenomenon of interdiffusion in BiSb alloy with neighbouring layers and interface chemistry to fully exploit the potential of BiSb based heterostructures for spintronic applications.

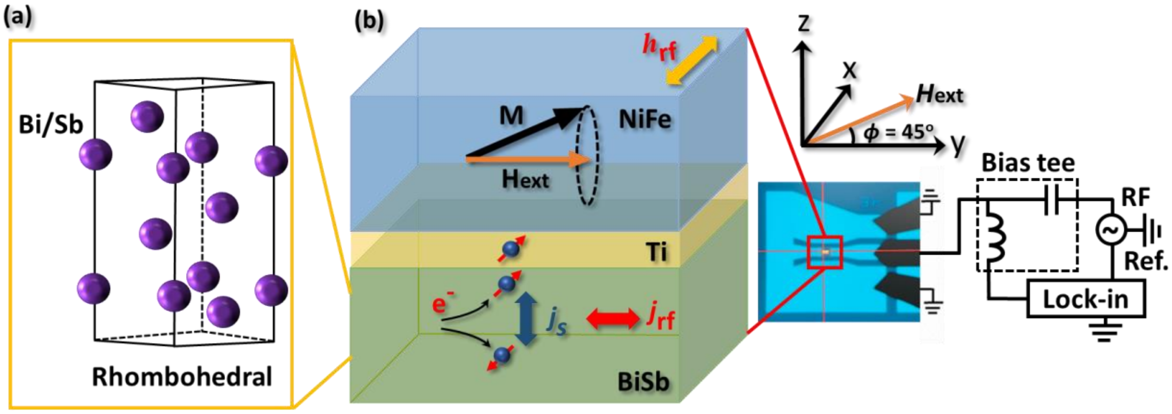

Figure 1. (a) Rhombohedral crystal structure of BiSb alloy; (b) Schematic representation of the multilayer stack of BiSb/Ti/NiFe, the photo image of coplanar waveguide device and the schematic of ST-FMR measurement set-up.

In this work, we have prepared conductive topological BiSb thin films with a ferromagnetic (FM) top layer of NiFe, investigated the effect of interfacial diffusion with and without a Ti insertion layer on the SOT efficiency under deposition, RT aging, and annealing conditions, and further analysed the detailed atomically resolved microstructures. Notably, the inclusion of a Ti spacer layer resulted in a significant enhancement of SOT efficiency in the as-deposited state. Intriguingly, this efficiency improvement persisted in the same sample after 45 days of RT aging and annealing at 400 K. This phenomenon can be understood as the modification of surface states through rearrangement of atoms and improved crystallinity of the BiSb layer. The microstructure analyses offered valuable insights into interface interdiffusion and the formation of compounds.

EXPERIMENTAL SECTION

Sapphire (c-plane) substrates were employed for the growth of BiSb thin films. The substrates were cleaned using the conventional cleaning process followed by the 1000 ºC annealing in a furnace. Thin films were grown from a $Bi_{85}Sb_{15}$ alloy target using DC magnetron sputtering. The composition of the deposited BiSb films was confirmed to be $Bi_{86}Sb_{14}$ by inductively coupled plasma analysis. All the depositions were done at RT. The growth process was carefully optimized to consider the fact that BiSb is highly susceptible to island growth. Thicknesses of the films are estimated using X-ray reflectivity measurements. Deposition rate of the BiSb is achieved to be 0.6 nm/s. Structural characterization of the BiSb films involved in-situ reflection high energy electron diffraction (RHEED) and X-ray diffraction (XRD). Atomic force microscopy (AFM) was utilized to capture the morphology of the films. Saturation magnetization of the stacks was extracted using a vibrating sample magnetometer (VSM) by carrying out the measurements in the in-plane (magnetic field) configuration. Four-probe resistivity measurements were conducted to understand the topological insulating nature of the BiSb films. Two stacks of BiSb/NiFe and BiSb/Ti/NiFe were deposited for a comparative study on the SOT efficiency. Coplanar wave guide devices were developed using conventional UV lithography to characterize SOT efficiency using spin-torque ferromagnetic resonance (ST-FMR). Figure 1(b) illustrates the schematic representation of the device stack, the spin transfer in the structure, the image of one device, and ST-FMR set up. We have considered 3 conditions for the samples S1 and S2, i.e., as-deposited, room temperature aged (45 days) and annealed (400 K). High-angle annular dark-field scanning transmission electron microscopy (HAADF-STEM) with energy dispersive X-ray spectroscopy (EDS) observations were carried for both as-deposited and annealed conditions of S1 and S2 samples to image the microstructures and observe the elemental distribution in the stacks. STEM investigation utilized the Titan G2 80–200 (FEI) at 200 kV, and cross-sectional STEM specimens were fabricated using the standard lift-out method with focused ion beam (FIB) and scanning electron microscopy (SEM) system Helios 5UX.

RESULTS & DISCUSSION

Characterization of the structure and resistivity of BiSb thin films

Figure 2(a) shows the RHEED pattern acquired immediately following the deposition of an 8 nm thick BiSb film. It reveals that the film was grown in the semi-polycrystalline regime, as evidenced by the distinctive semicircular arc-like features in the RHEED pattern. Subsequent annealing at 400 K induces discernible streaks in the RHEED pattern, as illustrated in Fig. 2(b), signifying an enhancement in crystallinity and the epitaxial growth of the BiSb thin film. The AFM image portrays the surface morphology of the BiSb film, with an estimated average roughness of 0.7 nm, indicating a remarkably flat film surface, as depicted in Fig. 2(c). The distinctive properties of the TSS in the BiSb thin films are elucidated through thickness-dependent resistivity measurements. Theoretically, TIs possess a bulk band gap akin to an insulator but with topologically protected conducting surface states. Consequently, with increasing the thickness of TIs, the insulating bulk contribution to the overall resistivity escalates. This phenomenon is observed in our BiSb films, where the resistivity demonstrates an incremental trend with film thickness (8, 10, 12 nm), as illustrated in Fig. 2(d). For the 4-nm thick film, a relatively elevated resistivity is noted, possibly attributable to the increased roughness of the film and the compromised surface state in the thin thickness regime. The measured minimum resistivity stands at 534 μΩ·cm, comparable to the values from prior studies.[26] The phase identification of the BiSb films was conducted via XRD measurements. Figure 2(f) shows XRD patterns of BiSb films with thicknesses of 4, 8, and 12 nm, respectively. In addition to diffraction peaks from the Al_2O_3(0001) substrate, peaks corresponding to (003), (006), and (009) lattice planes of BiSb emerge in the XRD results for BiSb (8 nm) and BiSb (12 nm). This is consistent with the epitaxial relationship between BiSb and sapphire substrates along the 0001 direction with a lattice mismatch of −4.9%. Conversely, the BiSb (4 nm) film exhibits weak intensity and a deteriorated texture, which could contribute to the heightened resistivity observed in the sample. These results suggest the existence of robust topological surface states in the BiSb films, particularly in films thicker than 8 nm, consistent with previous reports.[25]

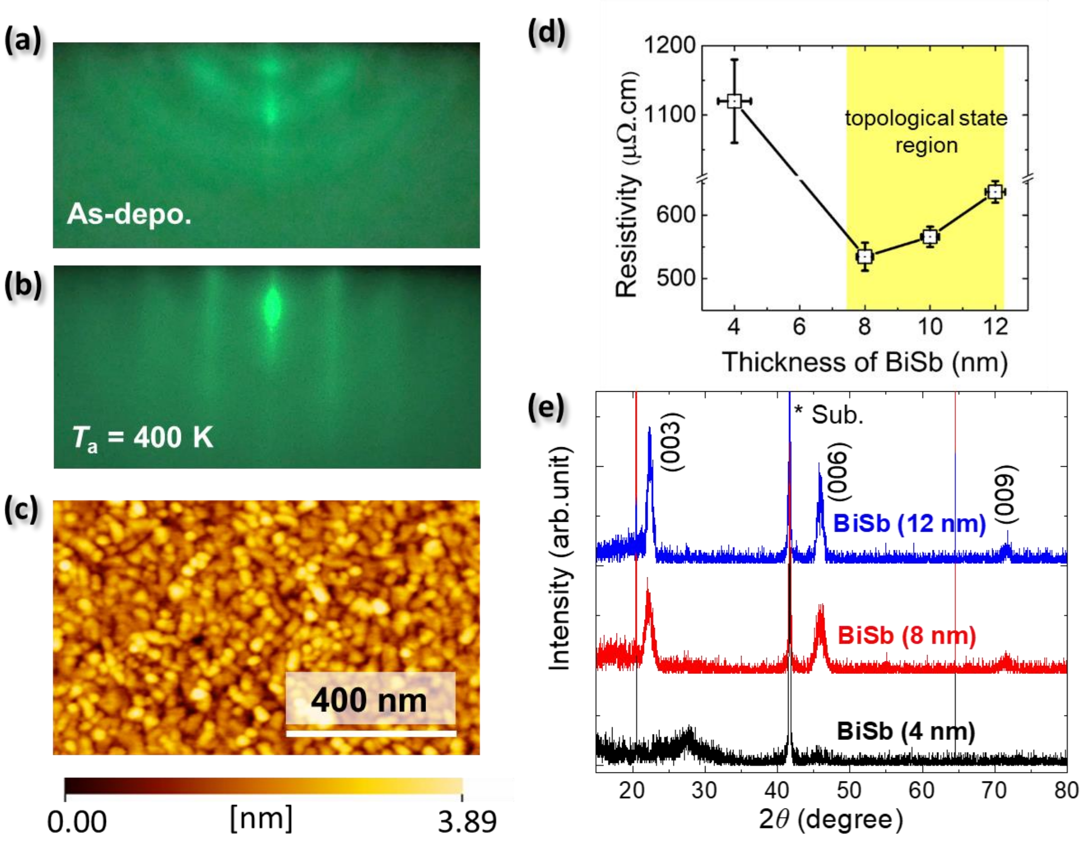

Figure 2. RHEED patterns of (a) as-grown and (b) 400 K annealed Al_2O_3//BiSb(8 nm), (c) AFM image capturing the surface morphology of Al_2O_3//BiSb(8 nm), (d) Resistivity as a function of BiSb thickness, showing the emergence of TSS (shaded region), (e) XRD of BiSb thin films with different thicknesses (4, 8, 12 nm). The measured samples in (c-e) are annealed.

Evaluation of SOT efficiencies

In order to investigate the SHE of the BiSb thin films, we grew a NiFe layer on the BiSb film, allowing for the assessment of SOT efficiency through ST-FMR measurements. Furthermore, we study the effect of interface on the SOT efficiency by introducing a Ti layer between BiSb and NiFe, as Ti is commonly employed in SOT heterostructures such as CoFeB/Ti and Co_2MnGa/Ti. The detailed stack structures are Al_2O_3(0001)//BiSb (8 nm)/NiFe (15 nm)/Cap for sample S1 and Al_2O_3(0001)//BiSb (8 nm)/Ti (2 nm)/NiFe (15 nm)/Cap for sample S2. XRD patterns of the samples S1 and S2 are presented in the Fig. S1 in the supporting information, which highlight the Ti spacer layer promotes the quality of BiSb in the entire stacks.

In ST-FMR measurements, the spin current generated by in the BiSb layer exerts a torque on the adjacent FM layer and excites magnetic precession, inducing a DC voltage signal through ferromagnetic resonance dynamics, which can be used to quantitatively evaluate the SOT efficiencies of these samples. Recent studies by Jiang *et al.* have shown a contribution of spin-torque-like signal from substrates in the ST-FMR measurements due to the rf current shunting into the substrate with high relative permittivity.[35] In our study, we employed an Al_2O_3(0001) substrate, which has a very high resistivity compared to the BiSb (8 nm) and a low permittivity, thus avoiding as much as possible any artifacts caused by the substrate in the measurements. Figure 3(a) shows the ST-FMR spectra for S1(as-deposited) at frequencies from 8 to 16 GHz and $\varphi = 45°$. Each spectrum is a combination of symmetric (S) and asymmetric signals (A) originating from the SOTs and Oersted field, respectively. Linewidth (Δ), resonance field (H_o), symmetric and asymmetric voltage signals are extracted by fitting the ST-FMR spectra using the following equation[36],

$$V_{mix} = S\frac{\Delta^2}{\Delta^2+(H_{ext}-H_0)^2} + A\,\frac{\Delta(H_{ext}-H_0)}{\Delta^2+(H_{ext}-H_0)^2}. \qquad (1)$$

A typical fitting result based on Eq. (1) is shown in Fig. 3(c), where the frequency is 12 GHz. The estimation of damping constant (α) using the linewidth dependence of frequency through $\Delta = (2\pi\alpha/\gamma)f + \Delta_o$ is shown in Fig. 3(c), where γ is the gyromagnetic ratio and Δ_o is the inhomogeneous linewidth broadening. The demagnetization field ($4\pi M_{\mathrm{eff}}$) of the sample was extracted using the Kittel formula, i.e., $f = (\gamma/2\pi)\sqrt{H_o(H_o + 4\pi M_{eff})}$, as shown in Fig. 3(d). The α and $4\pi M_{\mathrm{eff}}$ were obtained to be 0.0052 and 10428 Oe, respectively. Further, the ST-FMR spectra were measured by changing the magnetic field direction at a constant frequency of 12 GHz to investigate the angular dependence of S and A. In Figure 3(e) and 3(f), both S and A follow the form of $\sin(2\varphi)\cos(\varphi)$, which is consistent with previous works.[6] ST-FMR measurements have also been carried out to the sample S2 (as-deposited). Figure 4(a) shows the ST-FMR spectra of S2 from 8 to 16 GHz. Δ, H_{o}, S and A are extracted by fitting the obtained spectra using Eq. (1) as shown in Fig. 4(b). A clear difference has been observed in the S/A ratio between S2 and S1. Estimation of the damping constant and the demagnetization field are shown in Figs. 4(c) and 4(d), respectively, resulting in $\alpha = 0.0054$ and $4\pi M_{\mathrm{eff}} = 10840$. Figures 4(e) and 4(f) show the φ dependence of S and A, respectively, and they are also well-fitted by $\sin(2\varphi)\cos(\varphi)$. Similar measurements and analyses were done for the samples S1(RT aged, annealed) and S2 (RT aged, annealed).

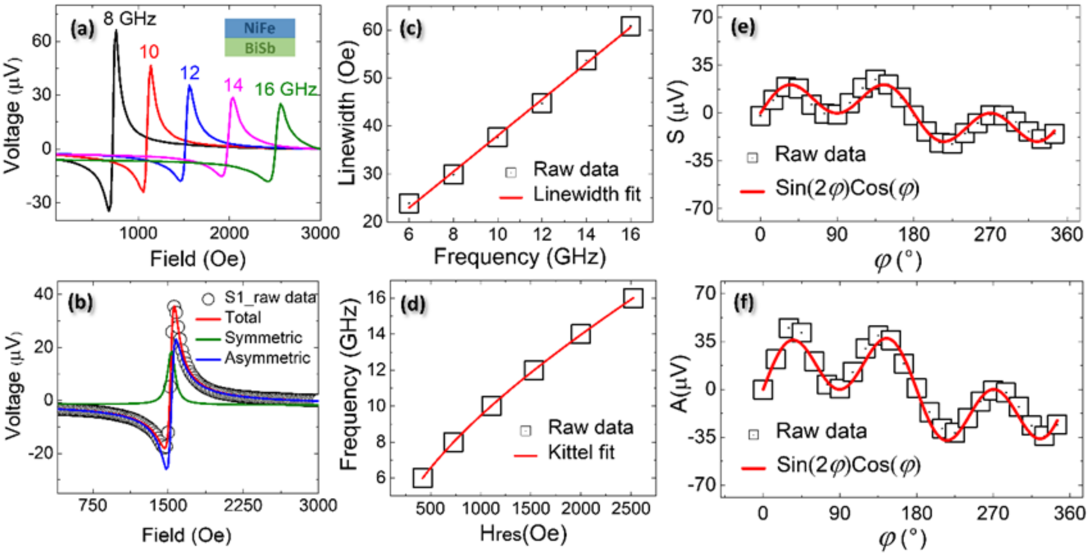

Figure 3. (a) ST-FMR spectra of S1(as-deposited), (b) A typical ST-FMR spectrum at 12 GHz with decomposed symmetric and anti-symmetric components using Eq. (1), (c) Linewidth of the ST-FMR spectra as a function of frequency and linear fit, (d) Resonance field (H_{res}) vs. frequency, and the solid line is the fit using the Kittel formula, (e) and (f) Angular dependencies of the symmetric and asymmetric components, fitted with sin(2φ)cos(φ) fits, respectively.

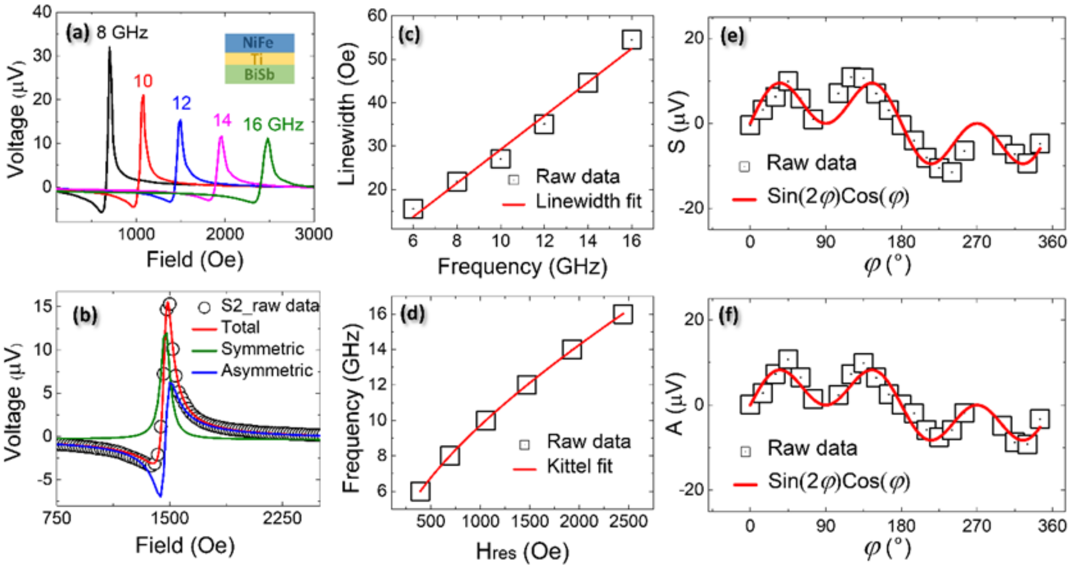

Figure 4. (a) ST-FMR spectra of S2 (as-deposited), (b) Decomposed symmetric and anti-symmetric components Symmetric of the ST-FMR spectrum at 12 GHz, (c) Linewidth of the ST-FMR spectra vs. Frequency, and the linear fit, (d) H_{res} vs. Frequency, and the Kittel fit, (e) and (f) Angular dependence of the S and A with sin(2φ)cos(φ) fits, respectively.

We further quantitatively evaluate the SOT efficiencies for these samples using the following equation[36],

$$\xi_{ST-FMR} = \frac{S}{A}\frac{e\mu_o M_s d_{BiSb} t_{NiFe}}{\hbar}\sqrt{1+\frac{4\pi M_{eff}}{H_o}}. \tag{2}$$

Here, d_{BiSb} is the thickness of BiSb, M_s is the saturation magnetization obtained from the magnetic hysteresis loops measured by VSM in Fig. S2 of the supporting information, and t_{NiFe} is the thickness of NiFe. The SOT efficiency in the case of S2 is achieved to be 0.84, which is around four times higher than 0.24 of the sample of S1 in the as-deposited condition. This enhancement could be understood as the Ti spacer layer protects the surface states of BiSb and eliminates the possibility of interdiffusion between BiSb and NiFe. Furthermore, we calculated the SOT efficiencies for the samples after RT aging for 45 days and post annealing at 400 K. Figure 5 shows the SOT efficiency values of all the conditions (i.e., as-deposited, RT aged, annealed) from S1 and S2 for comparison. Interestingly, the SOT efficiency of the sample S2 increases to 1 after aging and further increases to 1.2 after annealing, while the SOT efficiency of the sample S1 remains almost constant after aging and decreases after annealing. During aging and annealing, the rearrangement of the Bi and Sb atoms within BiSb layer may occur and improve the crystallinity and spin orbit coupling strength of the BiSb, which can in turn increase the SOT efficiency compared to the as-deposited case. Meanwhile, the insertion of Ti spacer layer in the sample S2 may hinder the atomic interdiffusion between the BiSb layer and the neighbouring NiFe layer. Whereas, for the sample S1 without Ti insertion layer, the diffusion between BiSb and NiFe may become severe after aging and annealing, thus affecting the SOT efficiency. Detailed microstructural analyses of the samples are shown in the following section.

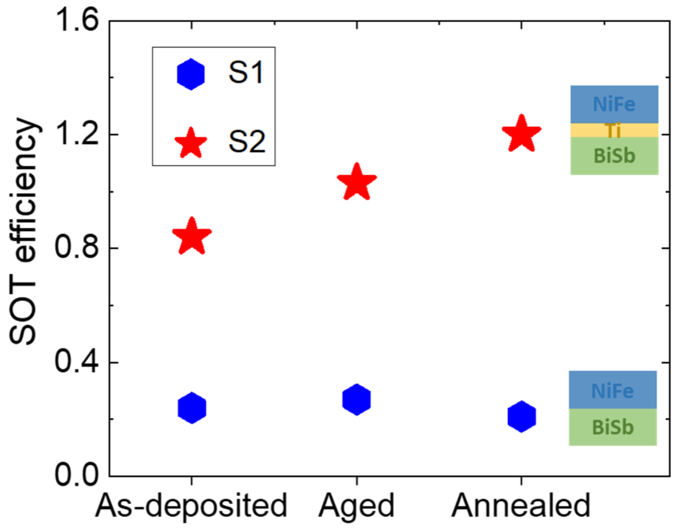

Figure 5. SOT efficiencies of samples S1 and S2 in as-deposited, RT aged, and annealed conditions, showing the comparison between S1 and S2 and the trend of SOT efficiency in different conditions.

Microstructural and elemental analysis

Cross-sectional STEM observations have been performed for the samples S1 and S2 of as-deposited and annealed conditions to understand and correlate the microstructure to the SOT efficiency. Figures 6(a) and 6(b) show the HAADF-STEM images of sample S1 in the as-deposited state and after annealing, respectively, which demonstrates the polycrystalline nature of BiSb in the case of S1 without a Ti spacer layer. After annealing, it is shown that there is a slight improvement in the crystallization of BiSb. A further improvement in crystallinity is observed in the HAADF-STEM images of sample S2 with Ti spacer layer from as-deposited to annealed, as shown in Figures 6(c) and 6(d). In particular, the BiSb layer in sample S2 under the annealing condition is more oriented/epitaxial compared to the samples under other conditions. We note that the crystal orientations of BiSb layers seem to be changed after annealing, especially for the case of the S2 sample. To clarify this, we extracted Fast Fourier Transform (FFT) patterns from the HAADF-STEM images, as shown in Fig. S3. The FFT patterns show that the differences come from different orientations in the TEM observations. While the difference in the S1 sample is due to different grains. The HAADF-STEM images of the wider regions are shown in Fig. S4 of the supporting information, which also demonstrates the clear difference in terms of the crystalline quality of the BiSb layer between S1 and S2 in the as-deposited and annealed conditions.

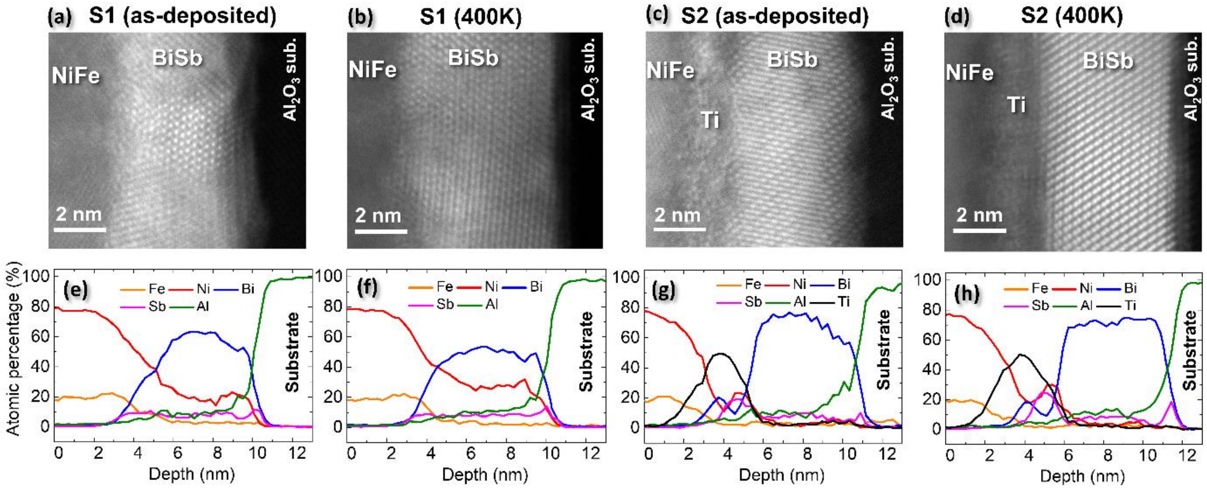

Figure 6. HAADF-STEM images of sample S1 (a) as-deposited and (b) annealed, and sample S2 (c) as-deposited, (d) annealed. EDS line profiles of sample S1 (e) as-deposited and (f) annealed, showing the interdiffusion of Ni, Sb, and Bi; (g) S2(as-deposited) and (h) S2(annealed) showing Ti as a diffusion barrier.

Figures 6(e-h) show the line profiles of STEM-EDS results for all the samples. Line profiles shown in Fig. 6(e) indicate a significant diffusion of Ni into the BiSb layer for the as-deposited sample S1. After annealing, the Ni diffusion becomes more pronounced as shown in Fig. 6(f). The diffusion of Ni can be understood as a result of the relatively high interatomic affinity of Ni with Bi and Sb. The phase diagrams of Ni-Bi and Ni-Sb show several regions of stable compounds between Ni and Bi, as well as Ni and Sb, at certain compositions [37,38], which suggests that the free energy for the formation of such compounds is responsible for the diffusion of Ni into the BiSb layer. The diffusion of Ni into BiSb could eventually destroy the topological insulating nature of the BiSb as this alters the composition of Bi and Sb which is essential for the existence of the topologically protected surface states. Thus, the destruction of topological properties due to the Ni diffusion leads to the reduction in SOT efficiency of the sample S1. Figures 6(g) and 6(h) show the elemental distributions in sample S2 (as-deposited and annealed) with Ti insertion layer. The elemental line profiles indicate that there is almost no diffusion of Ni into BiSb in both the as-deposited and annealed conditions, different from the situation for S1. Interestingly, we have observed a complex interface with the presence of Bi, Sb and Ni in the vicinity of Ti spacer layer. The formation of such interface could be due to the high chemical affinity of the elements according to the phase diagrams of Ti-Bi (Ti-Sb) where there are several stable alloying phases at some particular compositions, and thus these elements are more inclined to form alloying compounds at interfaces rather than solid solutions. The Ti insertion layer suppressed the diffusion of Ni into the BiSb layer, which also led to the high crystallinity of BiSb, especially after annealing, as shown in Fig. 6(d). By suppressing interdiffusion and improving crystallinity through the interfacial chemistry effect in the sample S2, the spin-orbit coupling arising from the topological electronic states could be preserved, resulting in robust spin transport and significantly increasing the SOT efficiency.

Regarding how the aging could enhance the spin transfer in both S1 and S2 heterostructures, we note that it is known that the sputtering process induces stresses in the thin films, depending on the mismatch between the substrate and the film, and the deposition rate, etc. In the case of alloys with low melting points, these stresses induced during the deposition tend to act as the driving force for the movement of species such that the overall system(film) comes to a stable minimum energy state. For samples S1 and S2 in aging condition, Bi and Sb move within the film and rearrange to form a stable phase with profound crystallinity, resulting in improved spin transport. In the case of an annealed sample of S2, as shown in Figure 6(d), the BiSb attains an epitaxial arrangement of atoms. As the crystallinity increases, the spin-orbit coupling strength of BiSb increases and the spin-charge conversion efficiency increases accordingly. Since profound crystallization is achieved by the annealing process, the annealed samples don’t show a similar aging effect. We also note that BiSb alloys have been reported to exhibit the quantum spin Hall effect (QSHE)[39,40], and the deposition of a ferromagnetic layer on a BiSb film may break the time-reversal symmetry at the interface and degrade the metallic state of BiSb[41]. Taking these into account, the SOT efficiency in our material systems may also partially originate from interfacial effects[42,43] and extrinsic scattering mechanisms[44] induced by the complex compounds at the interface due to interfacial chemistry.

CONCLUSION

In summary, we fabricated textured BiSb thin films and incorporated a Ti insertion layer in the BiSb/NiFe heterostructures. The investigation of SOT efficiencies was conducted across samples with and without Ti insertion, spanning as-deposition, RT aging, and annealing conditions. Remarkably, the sample featuring Ti insertion exhibited a significantly elevated SOT efficiency of approximately 1.2, surpassing that of the BiSb/NiFe without a Ti spacer layer by a factor of 4. Microstructural analyses revealed that the interface chemistry near the Ti spacer layer played a crucial role in impeding the interdiffusion of Bi/Sb and Ni atoms. This phenomenon can be attributed to the high interatomic affinity between these elements. Additionally, the crystallinity of the BiSb layer was notably enhanced in the Ti-inserted sample. These findings offer valuable insights into the intricate interfacial microstructures, underscoring the pivotal role of the Ti spacer layer in preserving the topological electronic states of BiSb and enhancing SOT efficiency. This study may pave a way for the realization of the practical application of BiSb-based topological materials in the field of spintronics.

■ ASSOCIATED CONTENT

Supporting Information

XRD patterns of the entire stacks of samples S1 and S2. Magnetic hysteresis (*M*-*H*) loops of the samples S1 and S2 measured by from VSM. HAADF-STEM images show wide areas of BiSb, NiFe and Ti layers.

■ AUTHOR INFORMATION

Corresponding Authors

Zhenchao Wen − National Institute for Materials Science, Tsukuba 305-0047, Japan; orcid.org/0000-0001-7496-1339; Email: WEN.Zhenchao@nims.go.jp

Authors

Talluri Manoj − Department of Materials Science and Metallurgical Engineering, Indian Institute of Technology-Hyderabad, 502284, Telangana, India.

Jun Uzuhashi − National Institute for Materials Science, Tsukuba 305-0047, Japan.

Tadakatsu Ohkubo − National Institute for Materials Science, Tsukuba 305-0047, Japan.

Hiroaki Sukegawa − National Institute for Materials Science, Tsukuba 305-0047, Japan.

Chandrasekhar Murapaka − Department of Materials Science and Metallurgical Engineering, Indian Institute of Technology-Hyderabad, 502284, Telangana, India.

Brian York − Western Digital, San Jose, CA 95119, USA.

Xiaoyong Liu − Western Digital, San Jose, CA 95119, USA.

Quang Le − Western Digital, San Jose, CA 95119, USA.

Seiji Mitani − National Institute for Materials Science, Tsukuba 305-0047, Japan.

Notes

The authors declare no competing financial interest.

■ ACKNOWLEDGMENTS

TM would like to thank Ministry of Human Resources and Development, India, and the IITH-NIMS Joint Center for materials science. CM would like to acknowledge funding from JICA Friendship 2.0.

■ REFERENCES

(1) Hsieh, D.; Xia, Y.; Wray, L.; Qian, D.; Pal, A.; Dil, J. H.; Osterwalder, J.; Meier, F.; Bihlmayer, G.; Kane, C. L.; Hor, Y. S.; Cava, R. J.; Hasan, M. Z. Observation of

Unconventional Quantum Spin Textures in Topological Insulators. *Science* **2009**, *323* (5916), 919–922.

(2) Fu, L.; Kane, C. L.; Mele, E. J. Topological Insulators in Three Dimensions. *Physical Review Letters* **2007**, *98* (10), 1–4.

(3) Culcer, D. Transport in Three-Dimensional Topological Insulators: Theory and Experiment. *Physica E: Low-Dimensional Systems and Nanostructures* **2012**, *44* (5), 860–884.

(4) Hsieh, D.; Qian, D.; Wray, L.; Xia, Y.; Hor, Y. S.; Cava, R. J.; Hasan, M. Z. A Topological Dirac Insulator in a Quantum Spin Hall Phase. *Nature* **2008**, *452* (7190), 970–974.

(5) Chi, Z.; Lau, Y. C.; Xu, X.; Ohkubo, T.; Hono, K.; Hayashi, M. The Spin Hall Effect of Bi-Sb Alloys Driven by Thermally Excited Dirac-like Electrons. *Science Advances* **2020**, *6*, eaay2324.

(6) Mellnik, A. R.; Lee, J. S.; Richardella, A.; Grab, J. L.; Mintun, P. J.; Fischer, M. H.; Vaezi, A.; Manchon, A.; Kim, E. A.; Samarth, N.; Ralph, D. C. Spin-Transfer Torque Generated by a Topological Insulator. *Nature* **2014**, *511* (7510), 449–451.

(7) Han, J.; Liu, L. Topological Insulators for Efficient Spin-Orbit Torques. *APL Materials* **2021**, *9*, 060901.

(8) Kharbouche-Harrari, M.; Alhalabi, R.; Postel-Pellerin, J.; Wacquez, R.; Aboulkassimi, D.; Nowak, E.; Prejbeanu, I. L.; Prenat, G.; Pendina, G. D. MRAM: From STT to SOT, for Security and Memory. *Proceedings - 33rd Conference on Design of Circuits and Integrated Systems, DCIS 2018* **2019**, 1–6.

(9) Prenat, G.; Jabeur, K.; Vanhauwaert, P.; Pendina, G. D.; Oboril, F.; Bishnoi, R.; Ebrahimi, M.; Lamard, N.; Boulle, O.; Garello, K.; Langer, J.; Ocker, B.; Cyrille, M. C.; Gambardella, P.; Tahoori, M.; Gaudin, G. Ultra-Fast and High-Reliability SOT-MRAM: From Cache Replacement to Normally-Off Computing. *IEEE Transactions on Multi-Scale Computing Systems* **2016**, *2* (1), 49–60.

(10) Prenat, G.; Jabeur, K.; Di Pendina, G.; Boulle, O.; Gaudin, G. Beyond STT-MRAM, Spin Orbit Torque RAM SOT-MRAM for High Speed and High Reliability Applications. In *Spintronics-based Computing*; Zhao, W., Prenat, G., Eds.; Springer International Publishing: Cham, 2015; pp 145–157.

(11) Huy, H. H.; Sasaki, J.; Khang, N. H. D.; Namba, S.; Hai, P. N.; Le, Q.; York, B.; Hwang, C.; Liu, X.; Gribelyuk, M.; Xu, X.; Le, S.; Ho, M.; Takano, H. Large Inverse Spin Hall Effect in BiSb Topological Insulator for 4 Tb/In2 Magnetic Recording Technology. *Appl. Phys. Lett.* **2023**, *122* (5), 052401.

(12) Garello, K.; Yasin, F.; Kar, G. S. Spin-Orbit Torque MRAM for Ultrafast Embedded Memories: From Fundamentals to Large Scale Technology Integration. *2019 IEEE 11th International Memory Workshop, IMW 2019* **2019**, 1–4.

(13) Saitoh, E.; Ueda, M.; Miyajima, H.; Tatara, G. Conversion of Spin Current into Charge Current at Room Temperature: Inverse Spin-Hall Effect. *Applied Physics Letters* **2006**, *88* (18), 15–18.

(14) Liu, J.; Ohkubo, T.; Mitani, S.; Hono, K.; Hayashi, M. Correlation between the Spin Hall Angle and the Structural Phases of Early 5d Transition Metals. **2015**, *107*, 232408.

(15) Kim, J.; Sinha, J.; Hayashi, M.; Yamanouchi, M.; Fukami, S.; Suzuki, T.; Mitani, S.; Ohno, H. Layer Thickness Dependence of the Current-Induced Effective Field Vector in Ta|CoFeB|MgO. *Nature Materials* **2013**, *12* (3), 240–245.

(16) Teo, J. C. Y.; Fu, L.; Kane, C. L. Surface States and Topological Invariants in Three-Dimensional Topological Insulators: Application to $Bi_{1-x}Sb_x$. *Phys. Rev. B* **2008**, *78*, 045426.

(17) Khang, N. H. D.; Ueda, Y.; Hai, P. N. A Conductive Topological Insulator with Large Spin Hall Effect for Ultralow Power Spin–Orbit Torque Switching. *Nature Materials* **2018**, *17* (9), 808–813.

(18) Checkelsky, J. G.; Hor, Y. S.; Cava, R. J.; Ong, N. P. Bulk Band Gap and Surface State Conduction Observed in Voltage-Tuned Crystals of the Topological Insulator Bi2Se3. *Physical Review Letters* **2011**, *106* (19), 4–7.

(19) Zhang, H.; Liu, C. X.; Qi, X. L.; Dai, X.; Fang, Z.; Zhang, S. C. Topological Insulators in Bi2Se3, Bi2Te3 and Sb2Te3 with a Single Dirac Cone on the Surface. *Nature Physics* **2009**, *5* (6), 438–442.

(20) Park, H.; Jeong, K.; Maeng, I.; Sim, K. I.; Pathak, S.; Kim, J.; Hong, S.-B.; Jung, T. S.; Kang, C.; Kim, J. H.; Hong, J.; Cho, M.-H. Enhanced Spin-to-Charge Conversion Efficiency in Ultrathin Bi_2Se_3 Observed by Spintronic Terahertz Spectroscopy. *ACS Appl. Mater. Interfaces* **2021**, *13* (19), 23153–23160.

(21) Dc, M.; Grassi, R.; Chen, J. Y.; Jamali, M.; Reifsnyder Hickey, D.; Zhang, D.; Zhao, Z.; Li, H.; Quarterman, P.; Lv, Y.; Li, M.; Manchon, A.; Mkhoyan, K. A.; Low, T.; Wang, J. P. Room-Temperature High Spin–Orbit Torque Due to Quantum Confinement in Sputtered BixSe(1–x) Films. *Nature Materials* **2018**, *17* (9), 800–807.

(22) Nguyen, M. H.; Pai, C. F. Spin-Orbit Torque Characterization in a Nutshell. *APL Materials* **2021**, *9* (3).

(23) Manchon, A.; Belabbes, A. *Spin-Orbitronics at Transition Metal Interfaces*, 1st ed.; Elsevier Inc., 2017; Vol. 68.

(24) Liu, L.; Pai, C. F.; Li, Y.; Tseng, H. W.; Ralph, D. C.; Buhrman, R. A. Spin-Torque Switching with the Giant Spin Hall Effect of Tantalum. *Science* **2012**, *336* (6081), 555–558.

(25) Nguyen, H.; Khang, D.; Nakano, S.; Shirokura, T.; Hai, P. N. Ultralow Power Spin – Orbit Torque Magnetization Switching Induced by a Non-Epitaxial Topological Insulator on Si Substrates. *Sci. Rep.* **2020**, *10*, 12185.

(26) Fan, T.; Tobah, M.; Shirokura, T.; Khang, N. H. D.; Hai, O. N. Crystal growth and characterization of topological insulator BiSb thin films by sputtering deposition on sapphire substrates. *Jpn. J. Appl. Phys.* **2020**, *59*, 063001.

(27) Sasaki, J.; Huy, H. H.; Khang, N. H. D.; Hai, P. N.; Le, Q.; York, B.; Liu, X.; Le, S.; Hwang, C.; Ho, M.; Takano, H. Improvement of the Effective Spin Hall Angle by Inserting an Interfacial Layer in Sputtered BiSb Topological Insulator (Bottom)/Ferromagnet with In-Plane Magnetization. *IEEE Trans. Magn.* **2022**, *58* (4), 2021–2024.

(28) Huy, H. H.; Ruixian, Z.; Shirokura, T.; Takahashi, S.; Hirayama, Y.; Hai, P. N. Integration of BiSb Topological Insulator and CoFeB/MgO with Perpendicular Magnetic Anisotropy Using an Oxide Interfacial Layer for Ultralow Power SOT-MRAM Cache Memory. *IEEE Trans. Magn.* **2023**, 59(11) 3400905.

(29) Ueda, Y.; Duy Khang, N. H.; Yao, K.; Hai, P. N. Epitaxial Growth and Characterization of $Bi_{1-x}Sb_x$ Spin Hall Thin Films on GaAs(111)A Substrates. *Appl. Phys. Lett.* **2017**, *110*, 062401.

(30) Khang, N. H. D.; Shirokura, T.; Fan, T.; Takahashi, M.; Nakatani, N.; Kato, D.; Miyamoto, Y.; Hai, P. N. Nanosecond Ultralow Power Spin Orbit Torque Magnetization Switching Driven by BiSb Topological Insulator. *Appl. Phys. Lett.* **2022**, *120*, 152401.

(31) York, B.; Hai, P.; Le, Q.; Hwang, C.; Nguyen, K.; Ho, H.; Sasaki, J.; Liu, X.; Le, S.; Ho, M.; Takano, H. The Practical Material Challenges Involved in Using the Topological Insulator BiSb in a Spin Transfer Device. *32nd Magnetic Recording Conference, TMRC 2021* **2021**, No. 012, 31–32.

(32) Poh, H. Y.; Ang, C. C. I.; Lim, G. J.; Jin, T. L.; Lee, S. H.; Koh, E. K.; Poh, F.; Lew, W. S. Crystallinity Control of the Topological-Insulator Surface $Bi_{85}Sb_{15}(012)$ via Interfacial Engineering for Enhanced Spin-Orbit Torque. *Phys. Rev. Appl.* **2023**, *19* (3), 034012.

(33) Rojas-Sánchez, J.-C.; Oyarzún, S.; Fu, Y.; Marty, A.; Vergnaud, C.; Gambarelli, S.; Vila, L.; Jamet, M.; Ohtsubo, Y.; Taleb-Ibrahimi, A.; Le Fèvre, P.; Bertran, F.; Reyren, N.; George, J.-M.; Fert, A. Spin to Charge Conversion at Room Temperature by Spin Pumping into a New Type of Topological Insulator: α -Sn Films. *Phys. Rev. Lett.* **2016**, *116* (9), 096602.

(34) Noel, P.; Thomas, C.; Fu, Y.; Vila, L.; Haas, B.; Jouneau, P.-H.; Gambarelli, S.; Meunier, T.; Ballet, P.; Attané, J. P. Highly Efficient Spin-to-Charge Current Conversion in Strained HgTe Surface States Protected by a HgCdTe Layer. *Phys. Rev. Lett.* **2018**, *120* (16), 167201.

(35) Jiang, D.; Chen, H.; Ji, G.; Chai, Y.; Zhang, C.; Liang, Y.; Liu, J.; Skowroński, W.; Yu, P.; Yi, D.; Nan, T. Substrate-Induced Spin-Torque-like Signal in Spin-Torque Ferromagnetic Resonance Measurement. *Phys. Rev. Applied* **2024**, *21* (2), 024021.

(36) Demasius, K.-U.; Phung, T.; Zhang, W.; Hughes, B. P.; Yang, S.-H.; Kellock, A.; Han, W.; Pushp, A.; Parkin, S. S. P. Enhanced Spin–Orbit Torques by Oxygen Incorporation in Tungsten Films. *Nat. Commun.* **2016**, *7* (1), 10644.

(37) Sheikhi, R.; Cho, J. Growth Kinetics of Bismuth Nickel Intermetallics. *J Mater Sci: Mater Electron* **2018**, *29* (22), 19034–19042.

(38) Cao, Z.; Takaku, Y.; Ohnuma, I.; Kainuma, R.; Zhu, H.; Ishida, K. Thermodynamic Assessment of the Ni-Sb Binary System. *Rare Metals* **2008**, *27* (4), 384–392.

(39) Fu, L.; Kane, C. L. Topological Insulators with Inversion Symmetry. *Phys. Rev. B* **2007**, *76* (4), 045302.

(40) Hsieh, D.; Qian, D.; Wray, L.; Xia, Y.; Hor, Y. S.; Cava, R. J.; Hasan, M. Z. A Topological Dirac Insulator in a Quantum Spin Hall Phase. *Nature* **2008**, *452* (7190), 970–974.

(41) Chang, C.-Z.; Wei, P.; Moodera, J. S. Breaking Time Reversal Symmetry in Topological Insulators. *MRS Bull.* **2014**, *39* (10), 867–872.

(42) Amin, V. P.; Zemen, J.; Stiles, M. D. Interface-Generated Spin Currents. *Phys. Rev. Lett.* **2018**, *121* (13), 136805.

(43) Song, J.; He, C.; Scheike, T.; Wen, Z.; Sukegawa, H.; Ohkubo, T.; Nozaki, Y.; Mitani, S. Charge-to-Spin Conversion in Fully Epitaxial Ru/Cu Hybrid Nanolayers with Interface Control. *Nanotechnology* **2023**, *34* (36), 365704.

(44) Cullen, J. H.; Culcer, D. Spin-Hall Effect Due to the Bulk States of Topological Insulators: Extrinsic Contribution to the Proper Spin Current. *Phys. Rev. B* **2023**, *108* (24), 245418.

For Table of Contents Use Only.